RSC Advances

ROYAL SOCIETY OF CHEMISTRY

PAPER

View Article Online
View Journal | View Issue

Check for updates

Cite this: *RSC Adv.*, 2026, **16**, 27057

Open Access Article. Published on 19 May 2026. Downloaded on 5/22/2026 12:58:10 PM.
This article is licensed under a Creative Commons Attribution-NonCommercial 3.0 Unported Licence.

An approach for the systematic profiling of drug-induced remodeling of RNA–RBP (RNA-binding protein) interactions

Yajie Jiao,[a] Jinguo Zhao,[a] Bin Fu,[a] Peiying Dong,[a] Xiaohong Qian,[a] Tong Liu*[ab] and Weijie Qin*[ac]

Received 1st February 2026
Accepted 4th May 2026

DOI: 10.1039/d6ra00871b

rsc.li/rsc-advances

Nucleic acid-based therapeutics targeting RNA-related regulatory networks have received substantial attention in drug development, among which the interventions of RNA–RBP (RNA-binding protein) interactions or RNA–protein complex assemblies represent a promising strategy for treating various diseases. RBPs play essential roles in post-transcriptional regulation, and their interactions with RNA are closely associated with physiological homeostasis and pathological progression. Although RNA–RBP interactions are increasingly recognized as therapeutic targets, the lack of systematic methods for screening the drugs that intervene in these interactions and evaluating their off-target effects remains a major bottleneck in the field. Here, we established an integrated approach combining biotinylated furocoumarin probe (BFP)-mediated RNA-tagging and RPC enrichment with quantitative proteomics to systematically profile the drug-induced remodeling of RNA–RBP interactions, thereby facilitating therapeutic drug discovery and off-target effect assessment. Applying this approach to MS-444-treated cells, we confirmed therapeutic target engagement by detecting inhibited HuR–RNA binding (the primary target of MS-444) and simultaneously revealed widespread binding suppression of RNA-processing RBPs, particularly those harboring RRM domains, as potential off-target effects. When applied to risdiplam-treated cells (an FDA-approved splicing modulator for spinal muscular atrophy), we verified the expected dissociation of hnRNP G from RNA transcripts and revealed extensive remodeling of SR and hnRNP splicing factors involved in SMN2 exon 7 regulation, providing insights into both its therapeutic mechanism and potential off-target perturbations. We anticipate that this approach will serve as a powerful platform for screening the drugs targeting RNA–RBP interactions and evaluating their off-target effects, thereby advancing the development of RNA-targeted therapeutics.

1. Introduction

The RNA-binding protein (RBP) is the key regulator of post-transcriptional gene expression in eukaryotic cells.[1] By assembling with RNA into RNA–protein complexes (RPCs), the RBP coordinates multiple steps of RNA metabolism, including processing, transport, translation, and degradation.[1–4] Under physiological conditions, the dynamic remodeling of RNA–RBP interactions is tightly controlled to maintain cellular homeostasis, while aberrant perturbations of these interactions are closely linked to the pathogenesis of numerous diseases, including cancer, neurodegenerative disorders, and genetic diseases.[5–8] For instance, the dysregulated binding of HuR to oncogenic mRNA 3′UTRs promotes tumor progression by enhancing mRNA stability and translation.[9–11] These findings highlight RNA–RBP interactions as attractive therapeutic targets for disease treatment. In recent years, nucleic acid-based therapeutics targeting RNA-related pathways have emerged as a rapidly developing field, with the interventions of RNA–RBP interactions representing a key direction.[12,13] Compared with traditional protein-targeted small molecules, the drugs that modulate RNA–RBP interactions directly target disease-related post-transcriptional regulatory networks, offering possibly higher therapeutic potential as seen in recent clinical successes.[14–16] For example, risdiplam (Evrysdi), the first FDA-approved oral small-molecule splicing modulator for spinal muscular atrophy (SMA), exerts its therapeutic effect by displacing hnRNP G from the SMN2 transcript and stabilizing U1 snRNP binding to the 5′ splice site of SMN2 exon 7, thereby promoting functional SMN protein expression.[16–18] However, the development of such therapeutics is severely hindered by two critical bottlenecks: first, the lack of systematic methods for

---

[a] *State Key Laboratory of Medical Proteomics, National Center for Protein Sciences Beijing, Academy of Military Medical Sciences, Beijing 102206, China. E-mail: liutong19920918@163.com; aunp_dna@126.com*

[b] *Key Laboratory of Engineering Biology for Low-Carbon Manufacturing, Systems Biology Centre, Technical Support Core Facilities, Tianjin Institute of Industrial Biotechnology, Chinese Academy of Sciences, Tianjin 300308, China*

[c] *Beijing Proteome Research Center, Beijing 102206, China*

© 2026 The Author(s). Published by the Royal Society of Chemistry

Open Access Article. Published on 19 May 2026. Downloaded on 5/22/2026 12:58:10 PM.
This article is licensed under a Creative Commons Attribution-NonCommercial 3.0 Unported Licence.

screening compounds that can specifically perturb the pathogenic RNA–RBP interactions. Second, the difficulty in comprehensively evaluating the off-target effects of these drugs, as RBP and RNA often form complex regulatory networks and non-specific perturbation may lead to unexpected side effects.[19,20] Although large-scale studies using metabolic RNA labeling and organic phase separation have revealed extensive RNA–RBP interactions in diverse biological contexts, current technologies are primarily focused on identifying biomolecular complexes rather than evaluating drug-induced perturbations, limiting their application in drug development.[21–25]

Mass spectrometry-based proteomics has been widely applied in drug discovery and target identification, including methods based on protein abundance changes, such as functional identification of targets by expression proteomics (FITExP), as well as methods relying on drug-induced alterations in protein stability, including thermal proteome profiling (TPP), solvent-induced protein precipitation (SIP), and pH-dependent protein precipitation (pHDPP).[26–29] Recent advances in matrix-augmented pooling strategy (MAPS) have further improved the throughput of stability-based target deconvolution, enabling multiplexed TPP for parallel deconvolution of multiple compounds, and revealed pronounced cell-specific drug–protein interaction landscapes.[30] Moreover, peptide-centric local stability assay (PELSA) has been developed to capture ligand-induced local stability shifts at the peptide level using limited proteolysis coupled with quantitative mass spectrometry.[31] However, these approaches are not suitable for studying drug-induced remodeling of RNA–RBP interactions since both RNA and drugs act as ligands affecting protein stability, making it difficult to distinguish direct perturbations of RNA–RBP interactions from indirect effects. Herein, we established an integrated workflow combining 254 nm UV-induced RNA and RBP crosslinking biotinylated furocoumarin probe (BFP)-mediated RNA tagging for RPC enrichment with quantitative proteomics to systematically characterize drug-induced remodeling of RNA–RBP interactions. This approach leverages furocoumarin-mediated RNA tagging and streptavidin–biotin affinity enrichment to specifically isolate RPCs followed by quantitative proteomics to compare RNA–RBP binding dynamics between drug-treated and untreated cells (Scheme 1). BFP integrates an RNA tagging moiety with an enrichment handle into a single molecule. Upon 365 nm UV irradiation, the 3,4-double bond of the pyrone ring and the 4′,5′-double bond of the furan ring in furocoumarin can undergo cycloaddition with the 5,6-double bond of the uracil base, resulting in the formation of cyclobutane adducts, thus avoiding non-specific side reactions with DNA or proteins and conferring high selectivity for RNA labeling.[32,33] The biotin moiety can specifically interact with streptavidin magnetic beads, thus allowing selective enrichment of the RPCs. We validated this approach using two model compounds: MS-444 (a potential anti-cancer compound targeting HuR–RNA interactions) and risdiplam (an FDA-approved SMA therapeutic targeting SMN2-related RNA–RBP interactions). For MS-444, we not only confirmed its therapeutic target *via* validating specific inhibition of HuR–RNA binding but also identified widespread binding suppression of other RNA-processing RBPs as potential off-target effects. For risdiplam, we verified the expected dissociation of hnRNP G from the SMN2 transcript and uncovered extensive remodeling of SR and hnRNP splicing factors involved in SMN2 exon 7 regulation, providing insights into its therapeutic mechanism and potential off-target perturbations. This study provides a powerful and generalizable platform for screening drugs that modulate RNA–RBP interactions and evaluating their off-target effects, thereby advancing the development of RNA-targeted therapeutics.

2. Experimental

2.1 Materials and reagents

MS-444 and risdiplam were purchased from MedChemExpress (New Jersey, USA). Biotinylated furocoumarin probe, HRP-conjugated streptavidin, Dynabead M-280 Streptavidin and RNase A (10 mg mL^{-1}) were purchased from Thermo Fisher Scientific (Waltham, USA). DEPC-treated water was obtained from Sangon Biotech (Shanghai, China). Ribonucleoside vanadyl complex (200 mM) was obtained from New England Biolabs (Ipswich, USA). Protease inhibitor cocktail tablets were purchased from Roche (Basel, Switzerland). Cell Counting Kit-8 (CCK-8) was purchased from Lablead Trading Co., Ltd (Beijing, China). Ultrapure RNA Kit and Protein Silver Stain Kit were ordered from CoWin Biosciences (Jiangsu, China).

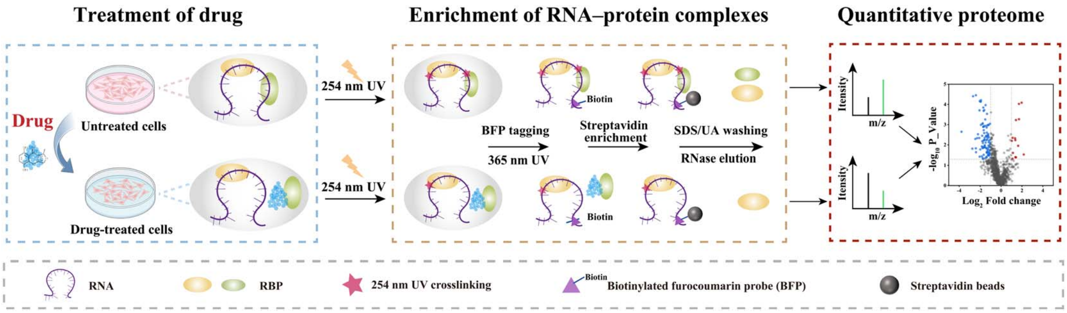

Scheme 1 Schematic overview of the integrated workflow for profiling the drug-induced remodeling of RNA–RBP (RNA-binding protein) interactions, combining biotinylated furocoumarin probe (BFP)-mediated tagging and enrichment of RNA–protein complexes (RPCs) with quantitative proteomic analysis.

© 2026 The Author(s). Published by the Royal Society of Chemistry

Open Access Article. Published on 19 May 2026. Downloaded on 5/22/2026 12:58:10 PM.
This article is licensed under a Creative Commons Attribution-NonCommercial 3.0 Unported Licence.

2.2 Cell culture and cell viability analysis

Human epithelial (HeLa), human colon cancer (HCT116) and human embryonic kidney (HEK293T) cell lines were obtained from the American Type Culture Collection (ATCC). Cells were cultured in Dulbecco's Modified Eagle's medium (DMEM) supplemented with 10% fetal bovine serum (FBS), 100 U mL^{-1} penicillin and 100 μg mL^{-1} streptomycin at 37 °C in a humidified atmosphere containing 5% CO_2.

For the cell viability analysis, HEK293T cells were seeded into 96-well plates at a density of 10^4 cells per well. After treatment with different concentrations of risdiplam for 24 h, the cells were incubated with 100 μL DMEM supplemented with 10 μL CCK-8 at 37 °C for 1 h. The absorbance at 450 nm was measured using a Multiskan MK3 microplate reader (Thermo Fisher Scientific, USA). Cell viability was calculated as: Cell viability (%) $= (A_t - A_m)/(A_u - A_m) \times 100\%$, where A_t, A_u, and A_m represent the absorbances of the risdiplam-treated cells, untreated cells, and medium-only control, respectively. At least three wells were tested per experiment.

2.3 Dot blotting analysis of photo-labeled RNA

Total RNA was extracted from the HeLa cells using an Ultrapure RNA Kit. A mixture containing 5 μg RNA and 5 μM BFP in 100 μL DEPC-treated water was exposed to 365 nm UV irradiation[32,34] at 20 mW cm^{-2} for 2 min using a UV LED instrument (UVSF81T, Futansi Electronic Technology, China), followed by an additional purification using the same kit. The labeled RNA was heated at 95 °C for 3 min, immediately cooled on ice, and spotted onto a nitrocellulose membrane (0.45 μm, Merck Millipore, Germany). Afterwards, the membrane was subjected to 254 nm UV exposure for 30 min to immobilize the RNA. Following washing with TBST for 5 min, the membrane was blocked with 5% (w/v) skim milk in TBST for 1 h and incubated with HRP-conjugated streptavidin (1 : 1000) for 1 h at RT. After washing three times with TBST for 10 min each, the membrane was incubated with ECL western blotting substrate and visualized using the ImageQuant LAS 500 system (Cytiva, USA).

2.4 Enrichment of RBPs from drug-treated cells

To evaluate the effects of MS-444, HCT116 cells were grown in 15 cm culture dishes to approximately 80% confluence, followed by treatment with 10 μM MS-444 in DMEM for 48 h. Vehicle-treated cells served as the negative control. After washing twice with PBS, cells were irradiated on ice with 254 nm UV[35–37] (0.25 J cm^{-2}) using a UV crosslinker (CL-1000, UVP, USA). Cells were harvested using a cell lifter and transferred to RNase-free centrifuge tubes. After centrifugation, the supernatant was discarded, and cell pellets were resuspended in 250 μL lysis buffer I (PBS, 0.5% SDS, 1× protease inhibitor, and 10 mM ribonucleoside vanadyl complex). The suspension was homogenized by repeated pipetting with a 1 mL syringe and incubated at 4 °C with gentle rotation for 30 min. Subsequently, 1 mL lysis buffer II (PBS, 0.1% Triton X-100, 1× protease inhibitor, and 10 mM ribonucleoside vanadyl complex) was added, followed by additional homogenization and incubation at 4 °C for 30 min. Lysates were centrifuged at 14 000*g* for 10 min, and the supernatant was transferred to a six-well plate. BFP was then added to the plate at a final concentration of 5 μM and incubated at 4 °C with shaking for 30 min. The plate was then irradiated on ice with 365 nm UV light (20 mW cm^{-2}) for 2 min. The supernatant was concentrated using Amicon Ultra centrifugal filters (10 kDa MWCO; Merck Millipore, Germany) and washed three times with PBS for buffer exchange. The BFP-treated lysate was adjusted to a volume of 500 μL with 2 M urea and incubated with 100 μL precleared streptavidin beads at 4 °C for 1 h with gentle rotation. Following magnetic separation and removal of the supernatant, the beads were washed twice with 200 μL PBS containing 0.2% SDS, twice with 200 μL PBS containing 8 M urea, and twice with 50 mM NH_4HCO_3. To release the RBPs, the beads were incubated with 20 μL RNase A (0.01 μg μL^{-1}) at 37 °C for 1 h. Eluates were collected for SDS-PAGE analysis or MS-based proteomic analysis. An RNase washing control was included, in which the cells and lysates were subjected to the same treatment except for an additional incubation with RNase A (0.1 μg μL^{-1}) at 37 °C for 1 h prior to the bead washing steps. All buffers used in this study were prepared using DEPC-treated H_2O. To evaluate the effects of risdiplam, HEK293T cells were incubated with 20.5 μM risdiplam in DMEM for 24 h, followed by RBP enrichment using the same procedure.

2.5 SDS-PAGE analysis of enriched RBPs

The eluted RBPs were denatured at 95 °C for 10 min in 1× SDS-PAGE loading buffer containing β-mercaptoethanol. The denatured proteins were separated on a 10% SDS-PAGE gel at 80 V for 20 min through the stacking gel and 120 V for 1 h through the resolving gel. The gel was then transferred to a clean container and silver-stained using Protein Silver Stain Kit to visualize protein bands.

2.6 Proteome sample preparation

2.6.1 RNA-binding proteome (RBPome) sample preparation. The eluted RBPs were reduced with 10 mM dithiothreitol (DTT) at 56 °C for 45 min and alkylated with 40 mM chloroacetamide (CAA) at room temperature for 45 min. The RBPs were digested by trypsin at a ratio of 50 : 1 (protein : enzyme) at 37 °C for 16 h. The resulting peptides were desalted using a StageTip C18, dried in a SpeedVac concentrator (Thermo Fisher Scientific, USA) and reconstituted in 100 μL of 100 mM tri-ethylammonium bicarbonate (TEAB) buffer. Stable isotope dimethyl labeling was performed for quantitative analysis. Briefly, the experimental samples were incubated with 8 μL of 4% (v/v) CH_2O, while RNase washing controls were incubated with 8 μL of 4% (v/v) CD_2O. Both experimental and control samples were supplemented with 8 μL of 0.6 M $NaBH_3CN$ and incubated for 1 h at room temperature. Reactions were quenched with 32 μL of 1% (v/v) ammonia solution and acidified with 16 μL of formic acid (FA). Following the mixing of the light-labeled and heavy-labeled peptides, the solution was desalted, dried and stored at −80 °C until LC-MS/MS analysis.

2.6.2 Whole-cell proteome sample preparation. Whole-cell lysates collected after 365 nm UV irradiation were prepared

Open Access Article. Published on 19 May 2026. Downloaded on 5/22/2026 12:58:10 PM.
This article is licensed under a Creative Commons Attribution-NonCommercial 3.0 Unported Licence.

using the filter-aided sample preparation (FASP) method.[38] Briefly, the lysates were transferred to 10 kDa filter units and centrifuged at 14 000*g* for 40 min. The filter units were then washed three times with 50 mM NH_4HCO_3 for buffer exchange and removal of low-molecular-weight components. Proteins in the filter units were reduced with 10 mM DTT at 37 °C for 4 h and alkylated with 40 mM CAA at room temperature for 45 min. After washing five times with 50 mM NH_4HCO_3, the proteins were digested with trypsin at a ratio of 50 : 1 (protein : enzyme) at 37 °C for 16 h. Subsequently, the peptide filtrates were collected by centrifugation at 14 000*g* for 10 min into new collection tubes. The peptide solutions were desalted, dried and stored at −80 °C until LC-MS/MS analysis.

2.7 LC-MS/MS analysis

2.7.1 LC-MS/MS analysis of RBPome sample. The dimethyl-labeled peptides were reconstituted in 0.1% FA and loaded onto a 150 μm i.d. × 15 cm reversed-phase column packed with 1.9 μm UltimateXB-C18 resin. Peptide separation was performed on an Easy nLC 1000 nano-LC system at a flow rate of 600 nL min^{-1} using a 78 min gradient: 5–8% B (0–8 min), 8–22% B (8–58 min), 22–32% B (58–70 min), 32–90% B (70–71 min), and 90% B (71–78 min). Solvent A consisted of 0.1% FA in water, and solvent B consisted of 0.1% FA in acetonitrile. The LC system was coupled to an Orbitrap Fusion Tribrid mass spectrometer (Thermo Fisher Scientific, USA) equipped with a nano-electrospray ionization source. The spray voltage was set to 2.0 kV, and the ion transfer tube temperature was maintained at 320 °C. Data were acquired in data-dependent acquisition (DDA) mode. Full MS scans (*m*/*z* 300–1400) were acquired in the Orbitrap at a resolution of 120 000 (AGC target of 5×10^5, maximum injection time 100 ms). Precursor ions were fragmented by higher-energy collision dissociation (HCD) with a normalized collision energy (NCE) of 32. MS2 spectra were acquired in the ion trap with an AGC target of 5×10^3, a maximum injection time of 35 ms, and a dynamic exclusion time of 18 s.

2.7.2 LC-MS/MS analysis of whole-cell proteome sample. Peptides were reconstituted in 0.1% FA and loaded onto a 75 μm i.d. × 20 cm reversed-phase column packed with 1.9 μm UltimateXB-C18 resin. Peptide separation was performed on an Easy nLC 1000 nano-LC system at a flow rate of 600 nL min^{-1} using a 120 min gradient: 7–12% B (0–8 min), 12–30% B (8–84 min), 30–42% B (84–109 min), 42–95% B (109–112 min), and 95% B (112–120 min). Solvent A consisted of 0.1% FA in water, and solvent B consisted of 0.1% FA in acetonitrile. The LC system was coupled to a Q Exactive HF mass spectrometer (Thermo Fisher Scientific, USA) equipped with a nano-electrospray ionization source. The spray voltage was set to 2.0 kV, and the ion transfer tube temperature was maintained at 320 °C. Data were acquired in data-independent acquisition (DIA) mode. Full MS scans (*m*/*z* 350–1200) were acquired in the Orbitrap at a resolution of 120 000 (AGC target of 3×10^6, maximum injection time 50 ms). Precursor ions were isolated using 60 fixed-width windows of 14.2 Da each and fragmented by HCD with an NCE of 25. MS2 spectra were acquired in the Orbitrap at a resolution of 30 000 with an AGC target of 1×10^6, and the maximum injection time was set to auto.

2.8 Mass spectrometry data analysis

2.8.1 Data analysis of RBPome sample. The raw files were searched using MaxQuant (version 2.0.3.0) against the UniProt KB/Swiss-Prot database (*Homo sapiens*, release 2025_04, 20 421 entries). Dimethyl labeling multiplicity was set to 2, with DimethLys0 and DimethNter0 as light labels and DimethLys4 and DimethNter4 as heavy labels. Trypsin was selected as the digestion enzyme with maximum two missed cleavages and minimum peptide length of six amino acids. Carbamidomethylation of cysteine was set as a fixed modification, while oxidation of methionine and N-terminal acetylation were set as variable modifications. For peptide identification, mass tolerances for precursor ions and fragment ions were set to 20 ppm and 0.5 Da, respectively. A false discovery rate (FDR) threshold of 1% was applied at both the peptide and protein levels. Missing values were imputed using the minimum value method in each dataset.[39] For RBP filtering, the processed data were imported into Perseus to compute the fold change (FC) between the experimental and RNase washing control groups, and statistical significance was determined by the Student's *t*-test with Benjamini–Hochberg (BH) correction. Proteins identified with at least two unique peptides in three tests and significantly enriched relative to the control (FC ≥ 2, BH-adjusted $P < 0.01$) were defined as RBPs.

2.8.2 Data analysis of whole-cell proteome sample. The raw files were searched using the DirectDIA workflow in Spectronaut (version 19.0) against the UniProt KB/Swiss-Prot database (*Homo sapiens*, release 2025_04, 20 421 entries). Trypsin was selected as the digestion enzyme with maximum two missed cleavages and minimum peptide length of six amino acids. Carbamidomethylation of cysteine was set as a fixed modification, while oxidation of methionine and N-terminal acetylation were set as variable modifications. An FDR threshold of 1% was applied at both the peptide and protein levels. Protein abundance data obtained from whole-cell lysates were first subjected to median normalization using the online BioLadder platform,[40] followed by the minimum value imputation method in each dataset.[39] RBPs exhibiting significant changes ($|FC| \geq 2$ and BH-adjusted $P < 0.05$) in protein abundance in the whole-cell proteome were excluded from the corrected analysis.

For the determination of drug-induced alterations in RNA binding, quantitative comparisons of RBPs between drug-treated and untreated cells were performed. In the quantitative proteomics workflow used to measure drug-induced alterations in RNA binding, a protein filtering step was applied before minimum value imputation and statistical testing, retaining only proteins quantified in at least two-thirds of the samples (4/6 runs) for downstream analysis. This type of valid-value filtering before imputation is commonly used in quantitative proteomics to reduce the impact of extensive missingness and improve the robustness of downstream statistical analysis.[41,42] The retained proteins were then subjected to median normalization to minimize batch effects[40] and minimum value

© 2026 The Author(s). Published by the Royal Society of Chemistry

Open Access Article. Published on 19 May 2026. Downloaded on 5/22/2026 12:58:10 PM. This article is licensed under a Creative Commons Attribution-NonCommercial 3.0 Unported Licence.

imputation to impute missing values.[39] After correcting by the global proteome level, RBPs meeting the criteria of $|FC| \geq 2$ and BH-adjusted $P < 0.05$ were classified as drug-altered RBPs.

2.9 Functional analysis of RBPs

Gene ontology (GO) enrichment analysis was performed using the DAVID database (https://davidbioinformatics.nih.gov/). Pathway enrichment analysis was conducted using Reactome (https://reactome.org/). Protein domain analysis was performed using SMART (https://smart.embl.de/). Protein–protein interaction (PPI) analysis was carried out using the STRING database (https://string-db.org/).

3. Results and discussion

3.1 Establishment of a workflow for screening RNA–RBP interaction modulators and evaluating off-target effects

To address the bottlenecks in drug development targeting RNA–RBP interactions, we established an integrated workflow for systematically profiling drug-induced remodeling of RNA–RBP interactions which can be used for both therapeutic candidate screening and off-target effect assessment (Scheme 1). The workflow consists of the following key steps. (1) Drug treatment: cells are treated with or without the candidate compound. (2) Crosslinking of RNA–RBP interactions: cellular RNA–RBP interactions are covalently crosslinked using 254 nm UV irradiation. (3) RPC enrichment: RNA within crosslinked RPCs is tagged with biotinylated furocoumarin probe (BFP) under 365 nm UV irradiation, and the RPCs are then isolated *via* streptavidin–biotin affinity purification. (4) False positive elimination: a stringent RNase washing is included in the control group to degrade its RNA, thereby removing all RNA-bound RBPs. In contrast, for the experimental group, non-RNase washing buffer was used to remove only non-specific background proteins. In this way, high-confidence RBPs are identified by a quantitative proteomics comparison between the experimental group and the RNase control using stable isotope dimethyl labeling (Fig. S1). (5) Quantitative analysis of RNA–RBP binding dynamics: quantitative proteomics is performed to compare the abundance of RBPs in RPCs between the drug-treated and untreated cells. To exclude the influence of global protein abundance changes induced by drug treatment, the measurements are corrected using whole-cell proteome data, ensuring that the observed differences specifically reflect remodeling of RNA–RBP interactions rather than changes in protein expression levels. This workflow enables systematic identification of RBPs whose RNA-binding is altered by drug

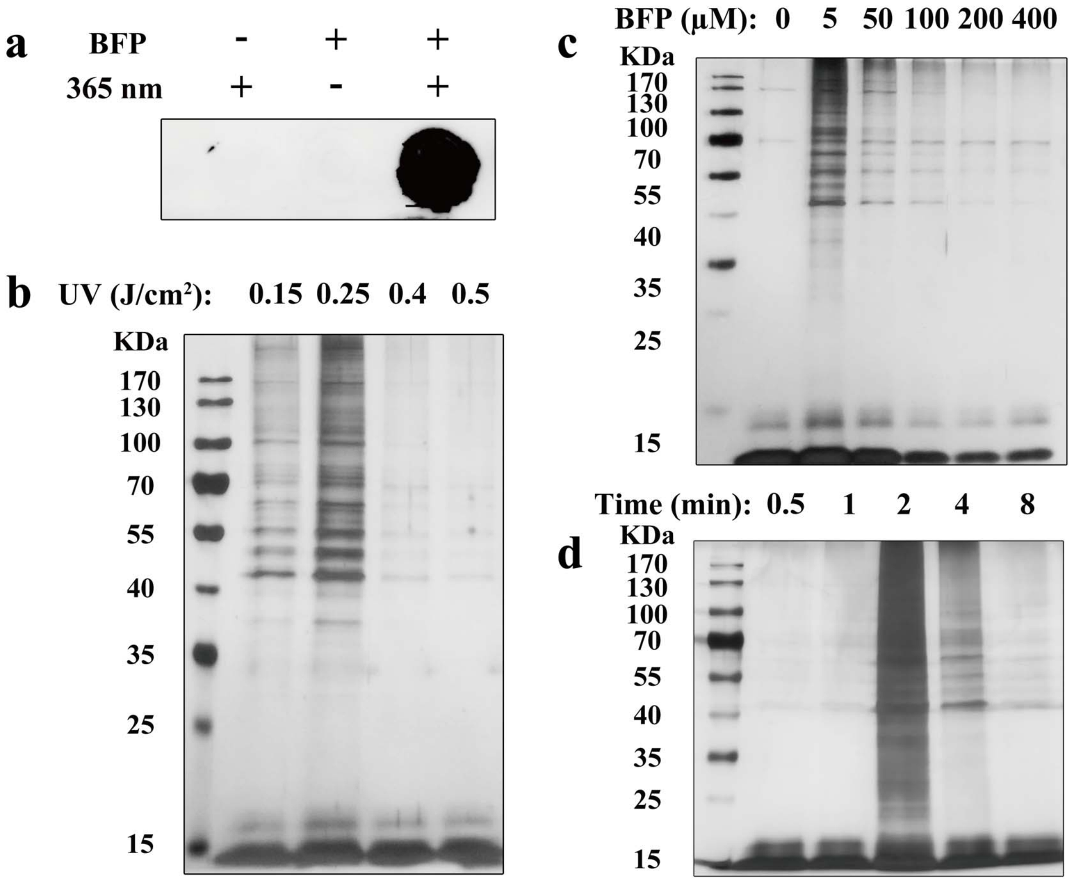

Fig. 1 Characterization and optimization of the RPC enrichment process. (a) Dot blot analysis detecting BFP labeling of the RNA extracted from HeLa cells under 365 nm UV irradiation. SDS-PAGE characterization of enriched RBPs under different conditions, including 254 nm UV irradiation dose (b), BFP concentration (c), and 365 nm UV labeling time (d).

Open Access Article. Published on 19 May 2026. Downloaded on 5/22/2026 12:58:10 PM.
This article is licensed under a Creative Commons Attribution-NonCommercial 3.0 Unported Licence.

treatment, thereby providing direct evidence for therapeutic target engagement and comprehensive information on potential off-target effects.

We first characterized and optimized the RPC enrichment process to ensure enrichment efficiency and specificity. Streptavidin dot blotting was used as a direct readout of RNA biotinylation. Using this assay, we confirmed that under 365 nm UV irradiation, the furocoumarin moiety of the BFP efficiently labeled the RNA molecules extracted from HeLa cells, generating a strong biotin signal. The absence of 365 nm UV or BFP resulted in complete abolition of the biotin signal, thereby validating the feasibility of the BFP-mediated RNA labeling with high selectivity (Fig. 1a). Next, we performed a series of optimization experiments at the protein level to maximize the recovery of crosslinked RPCs. Silver staining showed that the strongest protein bands were obtained when the 254 nm UV irradiation dose was set to 0.25 J cm^{-2}, the BFP concentration was 5 μM, and the 365 nm UV labeling time was 2 min (Fig. 1b–d). The choice of UV dose should be justified by considering both crosslinking efficiency and cell viability. UV dose–response curves for cell viability are shown in Fig. S2. Cell viability at 0.25 J cm^{-2} was not significantly different from that at 0.15 J cm^{-2}, whereas higher doses (0.4 and 0.5 J cm^{-2}) significantly reduced cell viability. Combined with the crosslinking efficiency results shown in Fig. 1b, 0.25 J cm^{-2} was selected as the irradiation condition for subsequent experiments as it maintained high cell viability while preserving good crosslinking efficiency. The above optimized parameters were adopted for subsequent experiments to enable reliable profiling RNA–RBP interactions.

3.2 MS-444-induced remodeling of RNA–RBP interactions: validation of therapeutic target and identification of off-target effects

We first applied the established workflow to evaluate MS-444, a chrysanthone-like compound reported to inhibit colorectal cancer (CRC) tumor growth by targeting HuR–RNA interactions.[43–45] HuR (ELAVL1) is an oncogenic RBP that binds to AU-rich elements (AREs) in the 3′UTRs of oncogenic mRNAs *via* its RRM domains, promoting mRNA stability and translation.[9,45–47] MS-444 is proposed to disrupt HuR–RNA interactions, but its off-target effects on other RNA–RBP interactions remain unknown. We treated HCT116 CRC cells with 10 μM MS-444 for 48 h (corresponding to the reported IC_{50} value)[44] and performed RBP enrichment and quantitative proteomics analysis.

The silver staining of the experimental group (without RNase washing) showed distinct RBP band patterns in the MS-444-treated and untreated samples, while these bands were almost absent in the RNase washing control, confirming the RNA-dependence of the enriched proteins and the high specificity of the BFP-based enrichment method (Fig. 2a). High-confidence RBPs were defined as proteins with fold enrichment ≥ 2 and BH-adjusted $P < 0.01$ compared to RNase controls. A total of 1369 high-confidence RBPs were identified from MS-444-treated and untreated cells (Table S1), 90.8% (1243) of which were annotated with the gene ontology term "RNA-binding" or previously reported as RBPs in large-scale human RBPome studies[21–25,48,49] (Fig. 2b and Table S2), confirming the reliability of the identified RBPs. Regarding the 9.2% non-overlapping proteins, a total of 126 proteins were not identified in previous large-scale human RBPome studies and were therefore retained as candidate RBPs. To systematically analyze these proteins, we compared them with the overlapping RBPs in terms of abundance and physicochemical properties. As shown in Fig. S3a, candidate RBPs (red dots) were more concentrated in regions with lower abundance compared to the overlapping RBPs (blue dots). Consistently, the median abundance of candidate RBPs (red box) in both the RBPome and the global proteome was lower than that of the overlapping RBPs (blue box), indicating that our BFP-based strategy has sufficient sensitivity to low-abundance RBPs and thus may have higher efficiency in in-depth RBPome analysis (Fig. S3b). The physicochemical characteristics of the candidate RBPs and overlapped RBPs were also compared, including hydrophobicity, positively charged amino acids, and disorder, and similar distribution patterns were found (Fig. S3c and d). Furthermore, several proteins of the candidate RBPs have independent literature support for RNA-related functions. For example, SIGMAR1 has been reported to interact with the 3′UTR of LC3B mRNA and promote its translation.[50] MRRF participates in post-termination dissociation of the ribosome from mRNA and facilitates ribosome recycling.[51] WDR74 is involved in early cleavage of pre-rRNA, particularly at ITS1 site 2, in cooperation with NVL2 and thereby contributes to ribosome biogenesis.[52] Taken together, these results suggest that the 9.2% non-overlapping proteins are potential candidate RBPs that were not identified previously, possibly due to their lower abundance. We also assessed the quantitative reproducibility of the identified RBPs across three technical replicates and observed good reproducibility with Pearson's correlation coefficients greater than 0.85 (Fig. 2c). Afterwards, we compared the BFP-based method with established RBP enrichment methods, including ChIRP-MS,[53] RAP-MS,[54] CARIC (4SU-based metabolic labeling)[55] and OOPS[56] (Table S3). This comparison highlights key metrics including specificity and throughput. Briefly, ChIRP-MS relies on formaldehyde crosslinking, which enriches both directly and indirectly RNA-associated proteins, resulting in lower specificity than the remaining RBP enrichment methods based on 254 nm UV crosslinking. CARIC relies on living cell metabolism for at least 18 hours to incorporate nucleoside analogs for RNA labeling before crosslinking, which limits its applicability to cell types with low uptake efficiency and may perturb normal RNA metabolism. In contrast, our BFP-based method does not rely on metabolic RNA labeling and combines 254 nm UV crosslinking and RNA-specific photo-labeling probes in a shortened enrichment workflow, enabling relatively high-throughput and high-specificity of RBP enrichment and therefore making it well suited for global RBPome profiling and analysis of perturbation-induced changes.

To characterize the MS-444-induced remodeling of RNA–RBP interactions, we compared the abundance of RBPs in RPCs between MS-444-treated and untreated cells (corrected by whole-cell proteome data). In the whole-cell proteome dataset,

© 2026 The Author(s). Published by the Royal Society of Chemistry

Open Access Article. Published on 19 May 2026. Downloaded on 5/22/2026 12:58:10 PM.
This article is licensed under a Creative Commons Attribution-NonCommercial 3.0 Unported Licence.

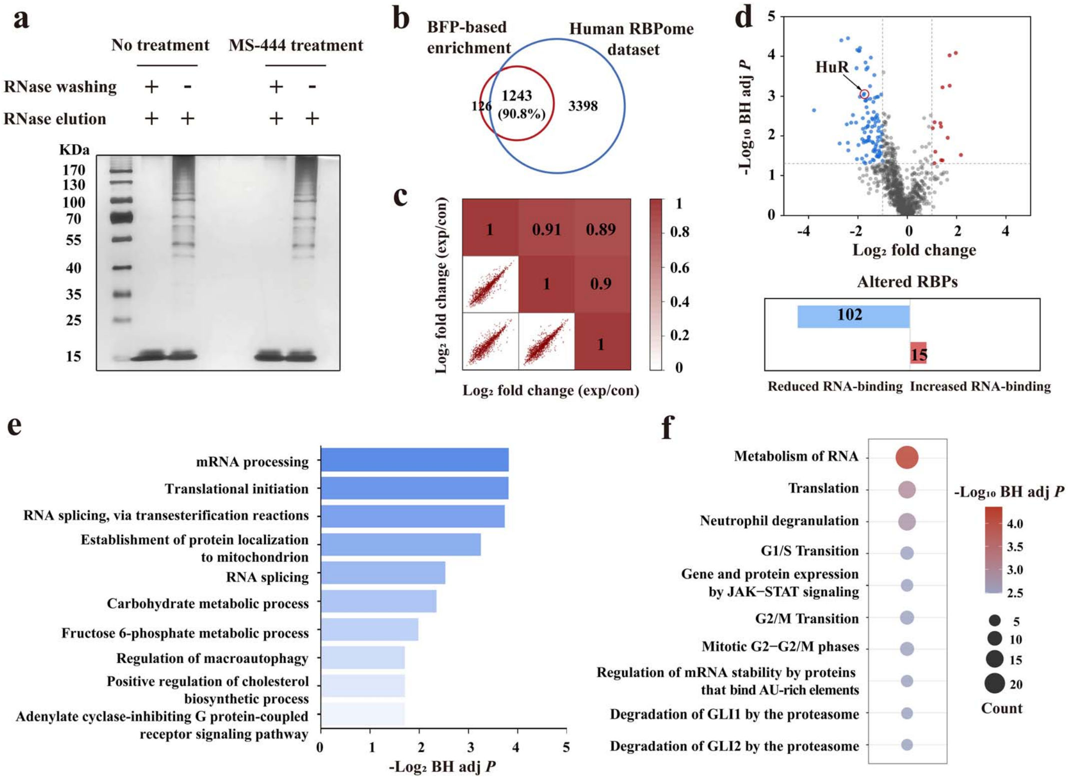

Fig. 2 Characterization of the BFP-based RNA-binding proteome and MS-444-induced remodeling of RNA–RBP interactions. (a) Silver staining of RBPs enriched by the BFP-based method with or without RNase A washing. (b) Venn diagram showing the overlap between the RBPs identified by BFP-based method and the reported RBP datasets derived from human cell lines. (c) Reproducibility assessment of RBPs enriched using the BFP-based method. (d) Volcano plot (upper panel) showing the $\log_2$ fold change (x-axis) and $-\log$ BH adjusted P values (y-axis) of RBPs between the MS-444-treated and untreated samples. Red and blue dots represent the RBPs with increased and reduced RNA-binding, respectively. Statistical analysis was performed using a two-sided Student's t-test (Benjamini–Hochberg adjusted P values) based on three biological replicates. Bar chart (lower panel) showing the number of significantly altered RBPs in the RNA-binding proteome upon MS-444 treatment. (e) Gene ontology enrichment analysis of biological process terms for the MS-444-induced RBPs with reduced RNA-binding. (f) Pathway enrichment analysis of the MS-444-induced RBPs with reduced RNA-binding.

a total of 8719 proteins were quantified in HCT116 cells (Table S4). We identified 117 significantly altered RBPs, among which 102 showed reduced RNA-binding and only 15 showed increased (Fig. 2d and Table S5). Notably, the known therapeutic target HuR exhibited a significant reduction in RNA-binding upon MS-444 treatment, consistent with the established mechanism of MS-444 inhibiting HuR–RNA interactions. This result confirms that our approach can reliably capture therapeutic target engagement, validating its utility in drug screening.

To evaluate the potential off-target effects of MS-444, we performed functional enrichment analysis of the 102 RBPs with reduced RNA-binding. Gene ontology enrichment analysis at the biological process level revealed significant overrepresentation of terms related to RNA processing and translation initiation (Fig. 2e), which are closely associated with the physiological function of HuR (stabilizing oncogenic mRNAs and promoting translation). Pathway analysis further highlighted significant enrichment of pathways involved in RNA metabolism, regulation of mRNA stability by proteins that bind AU-rich elements, and translation (Fig. 2f), indicating that MS-444 not only targets HuR but also perturbs a broader RNA–RBP interaction network involved in post-transcriptional regulation.

Since MS-444 recognizes HuR through its conserved RRM domains (the structural basis for RNA binding),[43,44] we hypothesized that other RBPs harboring structurally similar RRM domains may also be targeted by MS-444, leading to potential off-target effects. Domain analysis of the 102 RBPs with reduced RNA-binding identified six additional RRM-containing RBPs besides HuR, including EWSR1, HNRNPAB, SRSF10, PSPC1, U2AF2, and G3BP2 (Fig. 3a). Using the STRING database, protein–protein interaction (PPI) analysis mapped the RBPs with reduced RNA-binding into a HuR-interacting network comprising 17 nodes and 35 edges (Fig. 3b and Table S6). We identified a prominent module in the PPI network (blue nodes) displaying enriched RNA-related functions, including RNA metabolism and splicing. In addition, RBPs within the PPI network showed more significant reductions of RNA-binding compared to the overall reduced set. Similarly, RRM-containing RBPs were more strongly affected than non-RRM proteins (Fig. 3c). These results suggest that MS-444 may exhibit off-target effects by interacting with other RRM-containing RBPs within the HuR-interacting network, which is

© 2026 The Author(s). Published by the Royal Society of Chemistry

Open Access Article. Published on 19 May 2026. Downloaded on 5/22/2026 12:58:10 PM.
This article is licensed under a Creative Commons Attribution-NonCommercial 3.0 Unported Licence.

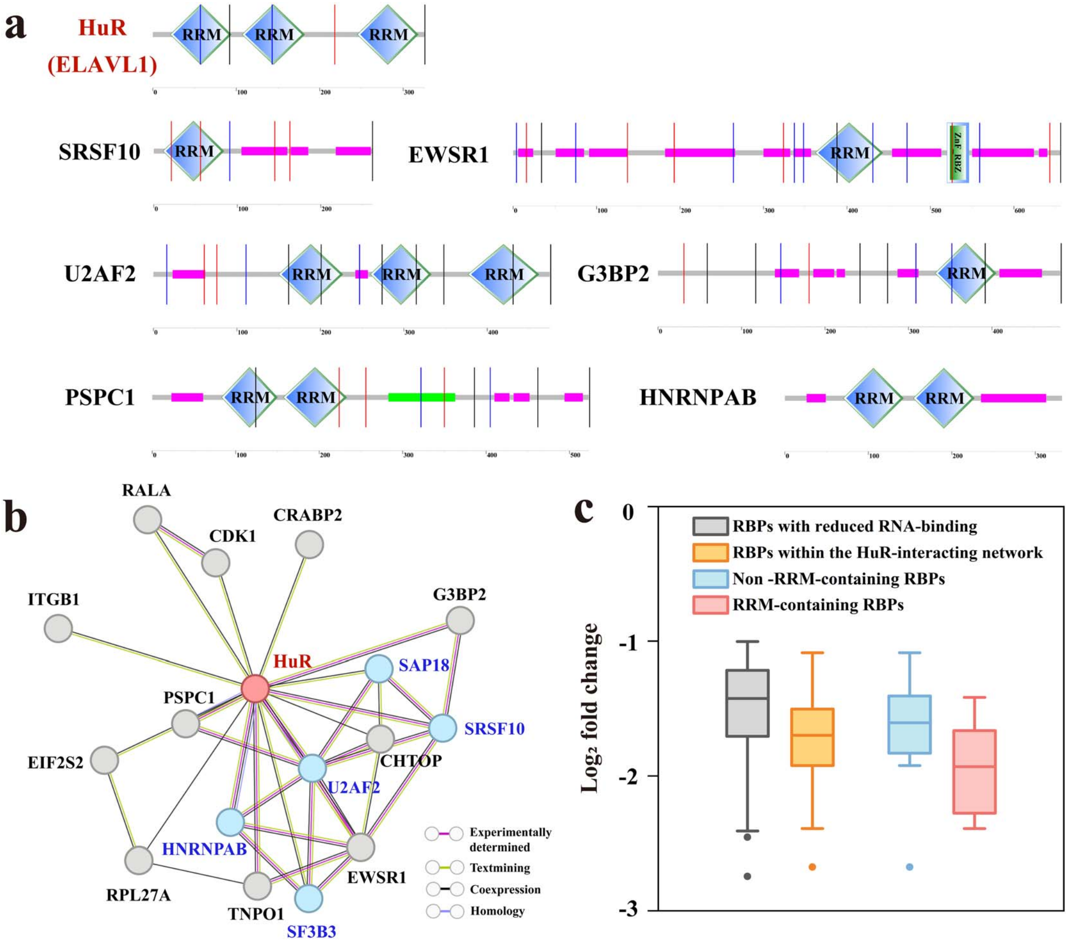

Fig. 3 Domain and PPI network analysis of the MS-444-induced RBPs with reduced RNA-binding. (a) Domain architecture of the RRM-containing RBPs with reduced RNA-binding using SMART. The blue diamonds indicate the RRM domains, the pink bars indicate the regions of low compositional complexity, and the green bars indicate the coiled-coil regions. The combined score integrates multiple evidence channels, including the experimentally determined interactions, text-mining, co-expression, and homology. (b) PPI network of the HuR-interacting RBPs constructed using STRING (interaction score > 0.4). (c) Box plots showing the distribution of $\log_2$ fold change for the RBPs with reduced RNA-binding, HuR-interacting RBPs, and RRM-containing RBPs.

likely due to the structural similarity of their RRM domains. This finding highlights the utility of our approach in identifying potential off-targets and elucidating the mechanisms of off-target effects, which is critical for optimizing drug specificity in therapeutic development.

3.3 Risdiplam-induced remodeling of RNA–RBP interactions: validation of therapeutic mechanism and off-target profiling

To further validate the utility of our approach in therapeutic evaluation, we applied it to risdiplam, an FDA-approved oral splicing modulator for SMA.[17,18] Risdiplam promotes SMN2 exon 7 inclusion and SMN protein expression by stabilizing the interaction between SMN2 exon 7 5′ splice site (5′ ss) and U1 snRNP and displacing hnRNP G from the exon splicing enhancer 2 (ESE2) region of SMN2 transcript.[57–61] While its therapeutic mechanism has been partially characterized, the global remodeling of RNA–RBP interactions induced by risdiplam (including potential off-target effects) remains unknown. We first evaluated the cell viability of risdiplam in HEK293T cells: cell viability was assessed after 24 h of treatment with increasing concentrations of risdiplam, and nonlinear curve fitting yielded an IC_{50} value of 20.5 μM (Fig. 4a). The rationale for choosing the IC_{50} was to balance biological efficacy with experimental interpretability, so that compound-induced RNA and RBP interaction changes could be robustly detected without using an arbitrarily high concentration. The adoption of IC_{50} as the reference concentration is widely accepted in pharmacological perturbation studies,[62,63] and therefore it was used for detecting drug-induced RNA and RBP interaction changes in this work. The IC_{50} obtained in our assay should be interpreted as an *in vitro* pharmacological parameter within this specific experimental context, not as a clinically predictive potency value. Consistent with this, previous studies in HEK293T-based systems used risdiplam at 0.1, 1.0, and 10 μM and observed concentration-dependent increases in SMN2 exon 7 inclusion, indicating that micromolar concentrations are commonly used for *in vitro* mechanistic interrogation even though they exceed clinical exposure levels.[64] Based on these considerations, cells

© 2026 The Author(s). Published by the Royal Society of Chemistry

Open Access Article. Published on 19 May 2026. Downloaded on 5/22/2026 12:58:10 PM.
This article is licensed under a Creative Commons Attribution-NonCommercial 3.0 Unported Licence.

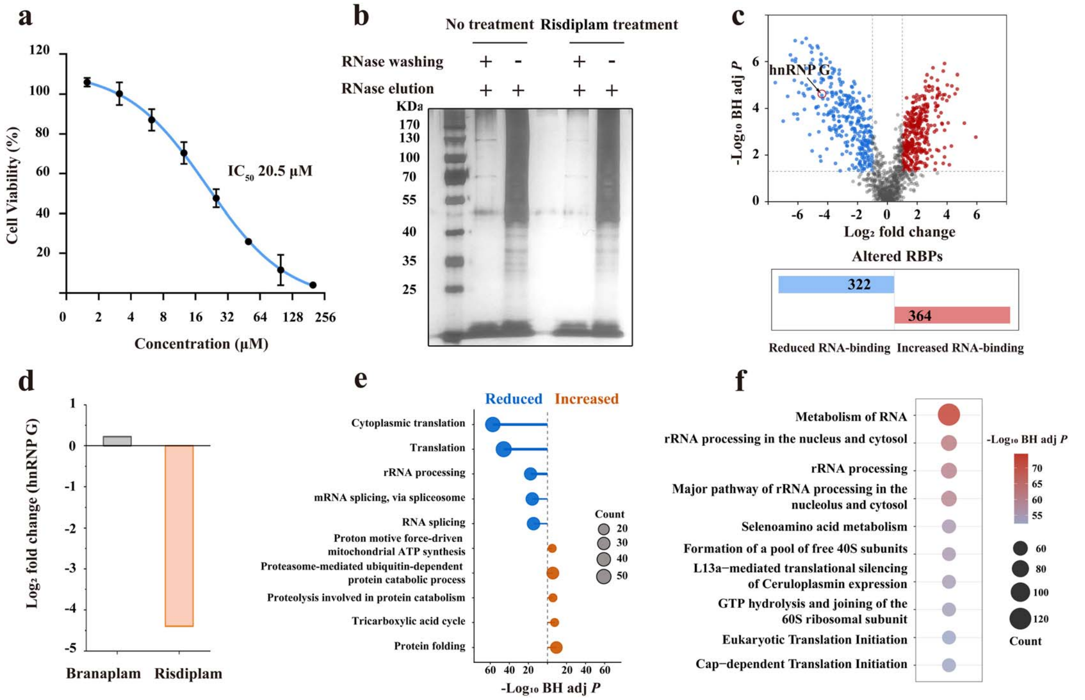

Fig. 4 Proteomic profiling of the risdiplam-induced remodeling of RNA–RBP interactions. (a) Cell viability dose–response curve of the HEK293T cells treated with increasing concentrations of risdiplam. (b) Silver staining of the RBPs enriched by the BFP-based method with or without RNase A washing. (c) Volcano plot (upper panel) showing $\log_2$ fold change (x-axis) and $-\log$ BH adjusted P values (y-axis) of the RBPs between risdiplam-treated and untreated samples. Bar chart (lower panel) showing the number of significantly altered RBPs in the RPCs upon risdiplam treatment. (d) Bar plot showing the $\log_2$ fold change of hnRNP G upon risdiplam and branaplam treatment. (e) GO enrichment analysis of biological process terms for the risdiplam-induced RBPs with increased and reduced RNA-binding. (f) Pathway enrichment analysis of the risdiplam-induced RBPs with reduced RNA-binding.

were treated with or without 20.5 μM risdiplam for subsequent RBP enrichment and quantitative proteomics analysis.

Silver staining showed prominent protein bands in the enriched RPC samples which were almost completely abolished in the RNase A washing control, confirming the RNA-dependence of the captured proteins (Fig. 4b). A total of 2047 high-confidence RBPs were identified across the risdiplam-treated and untreated cells (Table S7), 89.8% of which have been previously documented in human RBPome datasets.[21–25,48,49] In the whole-cell proteome dataset, a total of 8584 proteins were quantified in HEK293T cells (Table S8). Comparative quantification revealed 312 RBPs with reduced RNA-binding and 358 with increased binding (Fig. 4c and Table S9). Notably, hnRNP G (RBMX), the known target of risdiplam, showed a significant reduction in RNA-binding, consistent with the established mechanism of risdiplam-induced dissociation of hnRNP G from the SMN2 transcript. To confirm the specificity of this effect, we treated cells with branaplam, another SMA therapeutic with a distinct mechanism (primarily targeting 'MN2 5′ss without affecting hnRNP G),[60,61] and found that branaplam did not significantly alter hnRNP G-RNA association (Fig. 4d). This differential effect demonstrates that our approach specifically captures drug-induced perturbations of target RNA–RBP interactions, validating its utility in therapeutic mechanism validation. Additionally, the identification of numerous other altered RBPs provides a comprehensive profile of the potential off-target effects of risdiplam.

We next performed gene ontology enrichment analysis to characterize the functional roles of risdiplam-altered RBPs. For RBPs with reduced RNA-binding, biological process enrichment analysis revealed associations with translation, RNA splicing, and multiple RNA-processing events (Fig. 4e), which are closely related to the therapeutic mechanism of risdiplam (modulating SMN2 splicing). Pathway analysis further highlighted RNA metabolism-related pathways, including RNA processing, ribosome assembly, and translational regulation (Fig. 4f). In contrast, RBPs with increased RNA-binding were enriched in processes involving protein folding, cellular metabolism, and mitochondrial energy production (Fig. 4e), suggesting potential adaptive or compensatory responses of cells to risdiplam treatment. By comparing the RNA–protein interaction changes induced by risdiplam and branaplam, we identified a group of commonly downregulated RBPs, including those involved in ribosome-related and translational processes (RPS26, RPS27, RPL7A, RPL28), mitochondrial homeostasis and metabolism (DNM1L, CLUH, CLPB, PFKL), and chromatin and RNA regulatory processes (HMGB1, HELLS, ZNF326, ZC3HAV1, PTPN11, CUL3). This pattern may reflect broader remodeling of RNA–protein homeostasis, mitochondrial function, and cellular stress adaptation. Domain annotation showed that RBPs with reduced RNA-binding contain both classical RNA-binding domains (RRM, KH) and nonclassical domains (helicase C, SAP), with RRM as the most prominent category (Fig. 5a). Notably, several RRM-containing RBPs, including SR proteins

Open Access Article. Published on 19 May 2026. Downloaded on 5/22/2026 12:58:10 PM.
This article is licensed under a Creative Commons Attribution-NonCommercial 3.0 Unported Licence.

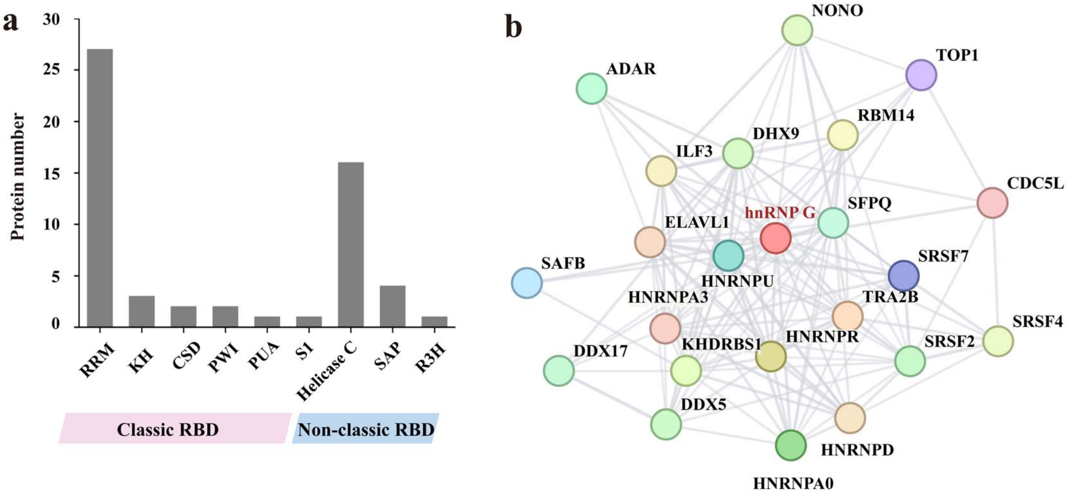

Fig. 5 Domain and PPI network analysis of the risdiplam-induced RBPs with reduced RNA-binding. (a) Domain classification of the RBPs with reduced RNA-binding based on classical and non-classical RNA-binding domains (RBDs) annotated by SMART. (b) PPI network of the hnRNP G-interacting RBPs constructed using STRING (interaction score > 0.7).

(SRSF2, SRSF4, SRSF7) and hnRNP family members (hnRNP A1, hnRNP Q, hnRNP M), are known regulators of SMN2 exon 7 splicing.[65–68] The altered RNA-binding of these RBPs suggests that the therapeutic effect of risdiplam on SMN2 splicing is not limited to displacing hnRNP G but involves coordinated remodeling of a broader network of splicing-related RNA–RBP interactions. PPI network analysis revealed that hnRNP G interacted with 22 other RBPs, many of which are core components of spliceosomal complexes or multifunctional RBPs involved in pre-mRNA processing (Fig. 5b). This indicates that risdiplam-induced dissociation of hnRNP G may propagate through its interaction network, leading to global changes in splicing-related RNA–RBP interactions. These findings not only deepen our understanding of the therapeutic mechanism of risdiplam but also identify potential off-target RBPs that may be involved in unintended splicing perturbations, providing critical information for clinical safety evaluation.

4. Conclusion

In this study, we established an integrated workflow for systematically profiling drug-induced remodeling of RNA–RBP interactions which addresses the key bottlenecks in the development of therapeutics targeting RPC assembly. By focusing on two model compounds (MS-444 and risdiplam), we demonstrated that this approach can reliably validate therapeutic target engagement (*e.g.*, MS-444 inhibiting HuR–RNA binding and risdiplam displacing hnRNP G), comprehensively profile potential off-target effects (*e.g.*, MS-444 perturbing RRM-containing RBPs in the HuR network and risdiplam altering splicing-related SR and hnRNP proteins), and deepen the understanding of therapeutic mechanisms. Compared with traditional proteomic methods, our approach specifically targets RNA–RBP interactions, enabling direct evaluation of drug efficacy and off-target risks associated with RNA–RBP interaction modulation. Future applications of this approach, combined with structural biology and computational modeling, may further enable rational design of highly specific drugs targeting RNA–RBP interactions.

Conflicts of interest

There are no conflicts to declare.

Data availability

The mass spectrometry proteomics data have been deposited to ProteomeXchange *via* the iProX partner repository with the dataset identifier PXD073833. Further inquiries can be directed to the corresponding authors.

Supplementary information (SI) is available. See DOI: https://doi.org/10.1039/d6ra00871b.

Acknowledgements

This study was supported by the National Key R&D Program of China (no. 2021YFA1302604), the National Natural Science Foundation of China (no. 32371504) and the State Key Laboratory of Proteomics Open Research Fund (no. SKLP-O202202 and SKLP-O202502).

References

1 S. He, E. Valkov, S. Cheloufi and J. Murn, *Nat. Rev. Genet.*, 2023, **24**, 276–294.
2 F. Gebauer, T. Schwarzl, J. Valcarcel and M. W. Hentze, *Nat. Rev. Genet.*, 2021, **22**, 185–198.
3 M. Corley, M. C. Burns and G. W. Yeo, *Mol. Cell*, 2020, **78**, 9–29.
4 H. Kim, C. Y. Cui, K. Toh, G. Ado, T. Ogawa, Y. X. Zhang, S. I. Sato, Y. B. Lim, H. Kurata, L. Zhou and M. Uesugi, *Chin. Chem. Lett.*, 2025, **36**, 110135.

Open Access Article. Published on 19 May 2026. Downloaded on 5/22/2026 12:58:10 PM.
This article is licensed under a Creative Commons Attribution-NonCommercial 3.0 Unported Licence.

5 S. Calabretta and S. Richard, *Trends Biochem. Sci.*, 2015, **40**, 662–672.

6 M. W. Hentze, A. Castello, T. Schwarzl and T. Preiss, *Nat. Rev. Mol. Cell Biol.*, 2018, **19**, 327–341.

7 A. Castello, B. Fischer, C. K. Frese, R. Horos, A.-M. Alleaume, S. Foehr, T. Curk, J. Krijgsveld and M. W. Hentze, *Mol. Cell*, 2016, **63**, 696–710.

8 X. J. You, L. Li, T. T. Ji, N. B. Xie, B. F. Yuan and Y. Q. Feng, *Chin. Chem. Lett.*, 2023, **34**, 107181.

9 S. S. Y. Peng, C. Y. A. Chen, N. H. Xu and A. B. Shyu, *EMBO J.*, 1998, **17**, 3461–3470.

10 L. E. Young, S. Sanduja, K. Bemis-Standoli, E. A. Pena, R. L. Price and D. A. Dixon, *Gastroenterology*, 2009, **136**, 1669–1679.

11 X. Q. Wu and L. Xu, *Adv. Drug Delivery Rev.*, 2022, **184**, 114179.

12 B. A. Taha, A. J. Addie, L. F. Z. Kolie, S. T. Wahhab, S. A. Abdulateef, A. J. Haider, K. Ibnaouf and N. Arsad, *Chin. Chem. Lett.*, 2026, **37**, 111955.

13 J. L. Guo, M. R. Gu, Y. H. Chen, T. Xiong, Y. Y. Zhang, S. M. Chen, M. L. Li, X. Q. Chen and X. J. Peng, *Chin. Chem. Lett.*, 2025, **36**, 110849.

14 C. M. McDonald, C. Campbell, R. E. Torricelli, R. S. Finkel, K. M. Flanigan, N. Goemans, P. Heydemann, A. Kaminska, J. Kirschner, F. Muntoni, A. N. Osorio, U. Schara, T. Sejersen, P. B. Shieh, H. L. Sweeney, H. Topaloglu, M. Tulinius, J. J. Vilchez, T. Voit, B. Wong, G. Elfring, H. Kroger, X. H. Luo, J. McIntosh, T. Ong, P. Riebling, M. Souza, R. J. Spiegel, S. W. Peltz, E. Mercuri, G. Clinical Evaluator Training and A. D. S. Grp, *Lancet*, 2017, **390**, 1489–1498.

15 M. Seiler, A. Yoshimi, R. Darman, B. Chan, G. Keaney, M. Thomas, A. A. Agrawal, B. Caleb, A. Csibi, E. Sean, P. Fekkes, C. Karr, V. Klimek, G. Lai, L. Lee, P. Kumar, S. C. W. Lee, X. Liu, C. Mackenzie, C. Meeske, Y. Mizui, E. Padron, E. Park, E. Pazolli, S. Y. Peng, S. Prajapati, J. Taylor, T. Teng, J. Wang, M. Warmuth, H. L. Yao, L. H. Yu, P. Zhu, O. Abdel-Wahab, P. G. Smith and S. Buonamici, *Nat. Med.*, 2018, **24**, 497–504.

16 G. Baranello, B. T. Darras, J. W. Day, N. Deconinck, A. Klein, R. Masson, E. Mercuri, K. Rose, M. El-Khairi, M. Gerber, K. Gorni, O. Khwaja, H. Kletzl, R. S. Scalco, T. Seabrook, P. Fontoura and L. Servais, *N. Engl. J. Med.*, 2021, **384**, 915–923.

17 J. Paik, *CNS Drugs*, 2022, **36**, 401–410.

18 T. Markati, G. Fisher, S. Ramdas and L. Servais, *Expert Opin. Invest. Drugs*, 2022, **31**, 451–461.

19 J. Jungfleisch and F. Gebauer, *RNA Biol.*, 2025, **22**, 1–8.

20 M. W. Hentze, P. Sommerkamp, V. Ravi and F. Gebauer, *Cell*, 2025, **188**, 4811–4827.

21 R. Huang, M. Han, L. Meng and X. Chen, *Proc. Natl. Acad. Sci. U. S. A.*, 2018, **115**, E3879–E3887.

22 X. Bao, X. Guo, M. Yin, M. Tariq, Y. Lai, S. Kanwal, J. Zhou, N. Li, Y. Lv, C. Pulido-Quetglas, X. Wang, L. Ji, M. J. Khan, X. Zhu, Z. Luo, C. Shao, D.-H. Lim, X. Liu, N. Li, W. Wang, M. He, Y.-L. Liu, C. Ward, T. Wang, G. Zhang, D. Wang, J. Yang, Y. Chen, C. Zhang, R. Jauch, Y.-G. Yang, Y. Wang, B. Qin, M.-L. Anko, A. P. Hutchins, H. Sun, H. Wang, X.-D. Fu, B. Zhang and M. A. Esteban, *Nat. Methods*, 2018, **15**, 213–220.

23 R. M. L. Queiroz, T. Smith, E. Villanueva, M. Marti-Solano, M. Monti, M. Pizzinga, D.-M. Mirea, M. Ramakrishna, R. F. Harvey, V. Dezi, G. H. Thomas, A. E. Willis and K. S. Lilley, *Nat. Biotechnol.*, 2019, **37**, 169–178.

24 J. Trendel, T. Schwarzl, R. Horos, A. Prakash, A. Bateman, M. W. Hentze and J. Krijgsveld, *Cell*, 2019, **176**, 391–403.

25 E. C. Urdaneta, C. H. Vieira-Vieira, T. Hick, H.-H. Wessels, D. Figini, R. Moschall, J. Medenbach, U. Ohler, S. Granneman, M. Selbach and B. M. Beckmann, *Nat. Commun.*, 2019, **10**, 990.

26 A. Chernobrovkin, C. Marin-Vicente, N. Visa and R. A. Zubarev, *Sci. Rep.*, 2015, **5**, 11176.

27 H. Franken, T. Mathieson, D. Childs, G. M. A. Sweetman, T. Werner, I. Toegel, C. Doce, S. Gade, M. Bantscheff, G. Drewes, F. B. M. Reinhard, W. Huber and M. M. Savitski, *Nat. Protoc.*, 2015, **10**, 1567–1593.

28 X. Zhang, Q. Wang, Y. Li, C. Ruan, S. Wang, L. Hu and M. Ye, *Anal. Chem.*, 2020, **92**, 1363–1371.

29 X. Zhang, K. Wang, S. Wu, C. Ruan, K. Li, Y. Wang, H. Zhu, X. Liu, Z. Liu, G. Li, L. Hu and M. Ye, *Chem. Sci.*, 2022, **13**, 12403–12418.

30 H. C. Ji, X. Lu, S. J. Zhao, Q. Q. Wang, B. Liao, L. G. Bauer, K. V. M. Huber, R. Luo, R. J. Tian and C. S. H. Tan, *Cell Chem. Biol.*, 2023, **30**, 1478–1487.

31 K. J. Li, S. J. Chen, K. Y. Wang, Y. Wang, L. J. Xue, Y. Y. Ye, Z. Fang, J. W. Lyu, H. Y. Zhu, Y. N. Li, T. Yu, F. Yang, X. L. Zhang, S. Q. Guo, C. F. Ruan, J. H. Zhou, Q. Wang, M. M. Dong, C. Luo and M. L. Ye, *Nat. Methods*, 2025, **22**, 278–282.

32 J. P. Calvet and T. Pederson, *Cell*, 1981, **26**, 363–370.

33 Y. Zhang, P. P. Y. Chan and A. E. Herr, *Angew. Chem., Int. Ed.*, 2018, **57**, 2357–2361.

34 P. L. Wollenzien, D. C. Youvan and J. E. Hearst, *Proc. Natl. Acad. Sci. U. S. A.*, 1978, **75**, 1642–1646.

35 J. R. Greenberg, *Nucleic Acids Res.*, 1979, **6**, 715–732.

36 A. J. Wagenmakers, R. J. Reinders and W. J. van Venrooij, *Eur. J. Biochem.*, 1980, **112**, 323–330.

37 J. Ule, K. B. Jensen, M. Ruggiu, A. Mele, A. Ule and R. B. Darnell, *Science*, 2003, **302**, 1212–1215.

38 J. R. Wiśniewski, A. Zougman, N. Nagaraj and M. Mann, *Nat. Methods*, 2009, **6**, 359–362.

39 Y. Jiang, A. Sun, Y. Zhao, W. Ying, H. Sun, X. Yang, B. Xing, W. Sun, L. Ren, B. Hu, C. Li, L. Zhang, G. Qin, M. Zhang, N. Chen, M. Zhang, Y. Huang, J. Zhou, Y. Zhao, M. Liu, X. Zhu, Y. Qiu, Y. Sun, C. Huang, M. Yan, M. Wang, W. Liu, F. Tian, H. Xu, J. Zhou, Z. Wu, T. Shi, W. Zhu, J. Qin, L. Xie, J. Fan, X. Qian and F. He, *Nature*, 2019, **567**, 257–261.

40 Y. Zhang, C. Yang, J. Wang, L. Wang, Y. Zhao, L. Sun, W. Sun, Y. Zhu, J. Li and S. Wu, *iMeta*, 2024, **3**, e215.

41 X. Zhang, A. H. Smits, G. B. van Tilburg, H. Ovaa, W. Huber and M. Vermeulen, *Nat. Protoc.*, 2018, **13**, 530–550.

42 W. Kong, H. W. H. Hui, H. Peng and W. W. B. Goh, *Proteomics*, 2022, **22**, e2200092.

© 2026 The Author(s). Published by the Royal Society of Chemistry

Open Access Article. Published on 19 May 2026. Downloaded on 5/22/2026 12:58:10 PM.
This article is licensed under a Creative Commons Attribution-NonCommercial 3.0 Unported Licence.

43 N.-C. Meisner, M. Hintersteiner, K. Mueller, R. Bauer, J.-M. Seifert, H.-U. Naegeli, J. Ottl, L. Oberer, C. Guenat, S. Moss, N. Harrer, M. Woisetschlaeger, C. Buehler, V. Uhl and M. Auer, *Nat. Chem. Biol.*, 2007, **3**, 508–515.

44 F. F. Blanco, R. Preet, A. Aguado, V. Vishwakarma, L. E. Stevens, A. Vyas, S. Padhye, L. Xu, S. J. Weir, S. Anant, N. Meisner-Kober, J. R. Brody and D. A. Dixon, *Oncotarget*, 2016, **7**, 74043–74058.

45 M. Lang, D. Berry, K. Passecker, I. Mesteri, S. Bhuju, F. Ebner, V. Sedlyarov, R. Evstatiev, K. Dammann, A. Loy, O. Kuzyk, P. Kovarik, V. Khare, M. Beibel, G. Roma, N. Meisner-Kober and C. Gasche, *Cancer Res.*, 2017, **77**, 2424–2438.

46 S. Lachiondo-Ortega, T. Cardoso Delgado, B. Banos-Jaime, A. Velazquez-Cruz, I. Diaz-Moreno and M. Luz Martinez-Chantar, *Cancers*, 2022, **14**, 2666.

47 N. Filippova, X. Yang, S. Ananthan, A. Sorochinsky, J. R. Hackney, Z. Gentry, S. Bae, P. King and L. B. Nabors, *J. Biol. Chem.*, 2017, **292**, 16999–17010.

48 A. Castello, B. Fischer, K. Eichelbaum, R. Horos, B. M. Beckmann, C. Strein, N. E. Davey, D. T. Humphreys, T. Preiss, L. M. Steinmetz, J. Krijgsveld and M. W. Hentze, *Cell*, 2012, **149**, 1393–1406.

49 A. Castello, B. Fischer, C. K. Frese, R. Horos, A. M. Alleaume, S. Foehr, T. Curk, J. Krijgsveld and M. W. Hentze, *Mol. Cell*, 2016, **63**, 696–710.

50 J. Knupp, Y. J. Chen, E. Wang, P. Arvan and B. Tsai, *Cell Rep.*, 2024, **43**, 114619.

51 E. Kummer, K. N. Schubert, T. Schoenhut, A. Scaiola and N. Ban, *Mol. Cell*, 2021, **81**, 2566–2582.

52 N. Hiraishi, Y. I. Ishida, H. Sudo and M. Nagahama, *Biochem. Biophys. Res. Commun.*, 2018, **495**, 116–123.

53 C. Chu, Q. C. Zhang, S. T. da Rocha, R. A. Flynn, M. Bharadwaj, J. M. Calabrese, T. Magnuson, E. Heard and H. Y. Chang, *Cell*, 2015, **161**, 404–416.

54 C. A. McHugh, C. K. Chen, A. Chow, C. F. Surka, C. Tran, P. McDonel, A. Pandya-Jones, M. Blanco, C. Burghard, A. Moradian, M. J. Sweredoski, A. A. Shishkin, J. Su, E. S. Lander, S. Hess, K. Plath and M. Guttman, *Nature*, 2015, **521**, 232–236.

55 R. Huang, M. Han, L. Meng and X. Chen, *Proc. Natl. Acad. Sci. U. S. A.*, 2018, **115**, E3879–e3887.

56 R. M. L. Queiroz, T. Smith, E. Villanueva, M. Marti-Solano, M. Monti, M. Pizzinga, D. M. Mirea, M. Ramakrishna, R. F. Harvey, V. Dezi, G. H. Thomas, A. E. Willis and K. S. Lilley, *Nat. Biotechnol.*, 2019, **37**, 169–178.

57 N. A. Naryshkin, M. Weetall, A. Dakka, J. Narasimhan, X. Zhao, Z. Feng, K. K. Y. Ling, G. M. Karp, H. Qi, M. G. Woll, G. Chen, N. Zhang, V. Gabbeta, P. Vazirani, A. Bhattacharyya, B. Furia, N. Risher, J. Sheedy, R. Kong, J. Ma, A. Turpoff, C.-S. Lee, X. Zhang, Y.-C. Moon, P. Trifillis, E. M. Welch, J. M. Colacino, J. Babiak, N. G. Almstead, S. W. Peltz, L. A. Eng, K. S. Chen, J. L. Mull, M. S. Lynes, L. L. Rubin, P. Fontoura, L. Santarelli, D. Haehnke, K. D. McCarthy, R. Schmucki, M. Ebeling, M. Sivaramakrishnan, C.-P. Ko, S. V. Paushkin, H. Ratni, I. Gerlach, A. Ghosh and F. Metzger, *Science*, 2014, **345**, 688–693.

58 S. Campagne, S. Boigner, S. Rudisser, A. Moursy, L. Gillioz, A. Knorlein, J. Hall, H. Ratni, A. Clery and F. H. T. Allain, *Nat. Chem. Biol.*, 2019, **15**, 1191–1198.

59 F. Malard, A. C. Wolter, J. Marquevielle, E. Morvan, A. Ecoutin, S. H. Rudisser, F. H. T. Allain and S. Campagne, *Nucleic Acids Res.*, 2024, **52**, 4124–4136.

60 M. Sivaramakrishnan, K. D. McCarthy, S. Campagne, S. Huber, S. Meier, A. Augustin, T. Heckel, H. Meistermann, M. N. Hug, P. Birrer, A. Moursy, S. Khawaja, R. Schmucki, N. Berntenis, N. Giroud, S. Golling, M. Tzouros, B. Banfai, G. Duran-Pacheco, J. Lamerz, Y. H. Liu, T. Luebbers, H. Ratni, M. Ebeling, A. Clery, S. Paushkin, A. R. Krainer, F. H. T. Allain and F. Metzger, *Nat. Commun.*, 2017, **8**, 1476.

61 Y. Ishigami, M. S. Wong, C. Marti-Gomez, A. Ayaz, M. Kooshkbaghi, S. M. Hanson, D. M. McCandlish, A. R. Krainer and J. B. Kinney, *Nat. Commun.*, 2024, **15**, 1880.

62 S. Aykul and E. Martinez-Hackert, *Anal. Biochem.*, 2016, **508**, 97–103.

63 A. Cortés, M. Cascante, M. L. Cárdenas and A. Cornish-Bowden, *Biochem. J.*, 2001, **357**, 263–268.

64 M. Uriostegui-Arcos, S. T. Mick, Z. Shi, R. Rahman and A. Fiszbein, *Nat. Commun.*, 2023, **14**, 3435.

65 C. D. Wee, M. A. Havens, F. M. Jodelka and M. L. Hastings, *PLoS One*, 2014, **9**, e115205.

66 T. Kashima, N. Rao, C. J. David and J. L. Manley, *Hum. Mol. Genet.*, 2007, **16**, 3149–3159.

67 H. H. Chen, J. G. Chang, R. M. Lu, T. Y. Peng and W. Y. Tarn, *Mol. Cell. Biol.*, 2008, **28**, 6929–6938.

68 S. Cho, H. Moon, T. J. Loh, H. K. Oh, S. Cho, H. E. Choy, W. K. Song, J. S. Chun, X. Zheng and H. Shen, *Biochim. Biophys. Acta, Gene Regul. Mech.*, 2014, **1839**, 306–315.

© 2026 The Author(s). Published by the Royal Society of Chemistry